AGU PUBLICATIONS

JGR

Journal of Geophysical Research: Planets

RESEARCH ARTICLE
10.1002/2013JE004486

Key Points:
- Radar observations probe below the surface of the lunar maria
- Radar echoes reveal details of lava flows and tectonic features
- Regolith thickness is 10–15 m in Mare Serenitatis

Correspondence to:
B. A. Campbell,
campbellb@si.edu

Citation:
Campbell, B. A., B. Ray Hawke, G. A. Morgan, L. M. Carter, D. B. Campbell, and M. Nolan (2014), Improved discrimination of volcanic complexes, tectonic features, and regolith properties in Mare Serenitatis from Earth-based radar mapping, *J. Geophys. Res. Planets*, *119*, 313–330, doi:10.1002/2013JE004486.

Received 24 JUL 2013
Accepted 28 DEC 2013
Accepted article online 5 JAN 2014
Published online 6 FEB 2014

Improved discrimination of volcanic complexes, tectonic features, and regolith properties in Mare Serenitatis from Earth-based radar mapping

Bruce A. Campbell[1], B. Ray Hawke[2], Gareth A. Morgan[1], Lynn M. Carter[3], Donald B. Campbell[4], and Michael Nolan[5]

[1]Smithsonian Institution, Center for Earth and Planetary Studies, Washington, District of Columbia, USA, [2]HIGP/SOEST, University of Hawai'i at Mānoa, Honolulu, Hawaii, USA, [3]NASA Goddard Space Flight Center, Greenbelt, Maryland, USA, [4]Department of Astronomy, Cornell University, Ithaca, New York, USA, [5]Arecibo Observatory, Arecibo, USA

Abstract Radar images at 70 cm wavelength show 4–5 dB variations in backscatter strength within regions of relatively uniform spectral reflectance properties in central and northern Mare Serenitatis, delineating features suggesting lava flow margins, channels, and superposition relationships. These backscatter differences are much less pronounced at 12.6 cm wavelength, consistent with a large component of the 70 cm echo arising from the rough or blocky transition zone between the mare regolith and the intact bedrock. Such deep probing is possible because the ilmenite content, which modulates microwave losses, of central Mare Serenitatis is generally low (2–3% by weight). Modeling of the radar returns from a buried interface shows that an average regolith thickness of 10 m could lead to the observed shifts in 70 cm echo power with a change in TiO_2 content from 2% to 3%. This thickness is consistent with estimates of regolith depth (10–15 m) based on the smallest diameter for which fresh craters have obvious blocky ejecta. The 70 cm backscatter differences provide a view of mare flow-unit boundaries, channels, and lobes unseen by other remote sensing methods. A localized pyroclastic deposit associated with Rima Calippus is identified based on its low radar echo strength. Radar mapping also improves delineation of units for crater age dating and highlights a 250 km long, east-west trending feature in northern Mare Serenitatis that we suggest is a large graben flooded by late-stage mare flows.

1. Introduction

Basaltic mare deposits comprise about 16% of the Moon's surface [*Head*, 1975]. Due to a combination of generally thin (<10 m) eruptive units and the smoothing effects of the regolith, distinct mare flow morphologies are rarely evident. Exceptions to this general behavior include 50–100 m thick, Eratosthenian period deposits in central Mare Imbrium [*Schaber*, 1973] and occasional flow lobes in other maria that are 10–30 m thick [*Gifford and El-Baz*, 1981]. Exposed layering in craters and pit walls, and estimates based on cooling models for basalt, suggest that many flow units are just 2–10 m thick [*Takeda et al.*, 1975; *Robinson et al.*, 2012]. Development of few kilometer scale basin fill thus implies hundreds to thousands of individual flows, likely of very low viscosity [e.g., *Weill et al.*, 1971; *Murase and McBirney*, 1973]. Collapse pits [*Robinson et al.*, 2012] suggest that plumbing systems similar to those in terrestrial basaltic volcanic fields contributed to the transport of magma over long distances.

The mare deposits are covered by an impact-generated regolith of fine-grained debris and rock fragments derived from the original lava flows. It is generally agreed that regolith thickness increases with age, so highland units have much deeper soil than mare units, but specific estimates of thickness in various locales differ widely based on photogeologic and remote sensing interpretations [e.g., *Oberbeck and Quaide*, 1968; *Quaide and Oberbeck*, 1968, 1975; *Shkuratov and Bondarenko*, 2001; *Wilcox et al.*, 2005; *Fa and Jin*, 2010]. Since flow morphology and soil thickness are not readily apparent, discrimination and mapping of mare units is often based on their Utraviolet-Visible (UV-VIS) reflectance properties, which vary strongly from "red" to "blue" due to differences in iron and titanium abundance and on their relative albedo that varies in part with the presence of opaque components in the soil; these relationships have been used to develop empirical models for TiO_2 and FeO abundance [e.g., *Lucey et al.*, 2000; *Le Mouelic et al.*, 2000; *Gillis et al.*, 2003; *Wu et al.*,

2012]. Additional information is provided by orbital gamma ray spectrometer (GRS) and neutron spectrometer (NS) compositional data at lower spatial resolution [*Elphic et al*., 2002; *Prettyman et al*., 2006]. Unit boundaries based on differences in reflectance properties are often adopted in assessing resurfacing ages based on impact crater populations [*Hiesinger et al*., 2000, 2003] and to understand the stratigraphy of mare-forming lavas [e.g., *Weider et al*., 2010].

Synthetic aperture radar mapping can probe beneath the surface of the lunar regolith with horizontal spatial resolution of tens to a few hundred meters. The depth of probing is determined by the radar wavelength, with longer wavelengths penetrating to greater depth and on the microwave loss properties of the target material. Early studies showed that radar echoes at 70 cm wavelength, because they arise in large part due to rocks suspended in the lossy soil, are strongly affected by regolith titanium content across Mare Imbrium [*Schaber et al*., 1975]. This conclusion was extended to other maria by *Campbell et al*. [1997]. With improved radar image spatial resolution at a range of wavelengths, it is possible to directly compare backscatter properties with UV-VIS and GRS/NS maps to assess regolith composition and thickness effects.

In a preliminary study, *Campbell et al*. [2009] showed that some variations in 70 cm radar backscatter strength and circular polarization ratio (CPR) for the maria are not fully explained by differences in TiO_2 abundance inferred from Clementine UV-VIS observations using the method of *Lucey et al*. [2000]. Regions of Maria Serenitatis, Crisium, and Imbrium have higher backscatter and CPR than expected, and exhibit variability in radar scattering within areas of almost uniform multispectral reflectance properties. These changes were not evident in the 12.6 cm wavelength radar images available at the time, suggesting that the 70 cm signals detect variations in rock abundance or microwave loss at least several meters below the regolith surface.

To build upon and understand these findings, we present new high-resolution, dual-polarization radar images of Mare Serenitatis at 70 cm and 12.6 cm wavelengths, using observing techniques described in section 2. Section 3 provides a simple model for radar attenuation and scattering in the regolith and revisits dielectric measurements of Apollo samples to focus on the dependence of microwave loss on mare regolith composition. Section 4 uses new radar and visible image data for Mare Serenitatis to map flow features evident at the longer wavelength, refine the definition of unit boundaries for relative age determination, and assess regolith thickness. Section 5 offers a model consistent with the backscatter differences and discusses geologic implications for the patterns observed in the radar maps.

2. Radar Data Sets

We acquired the 70 cm wavelength (430 MHz frequency) radar images of Mare Serenitatis presented here on 12–13 September 2009. The observing strategy follows that described in *Campbell et al*. [2007], using the transmitter at the Arecibo Observatory in Puerto Rico and receivers at the Green Bank Telescope in West Virginia. The transmitted signal is circularly polarized, and we receive echoes in both the same sense (SC) and opposite sense (OC) of circular polarization. The circular polarization ratio (CPR = SC/OC) is similar to the SC echo strength in its sensitivity to diffuse scattering from rocks and can be calibrated to an accuracy of a few percent from measurement of the receiver noise in each channel, which is dominated by thermal emission from the Moon [*Campbell et al*., 2007, 2010; *Campbell*, 2012].

To achieve the best possible spatial resolution along the range axis, we used a 1 μs baud (the equivalent time resolution and lower limit of the transmitter) modulated by a 13-element Barker code [*Evans*, 1968]. The coherent integration time for each mapping look is 33 min, yielding approximately 225 m horizontal spatial resolution along the frequency axis. The horizontal resolution along the range axis is 200 m to 250 m. We map each look to backscattered power at a 200 m spacing and sum multiple looks to reduce speckle in the final image; the Mare Serenitatis observations comprise seven such independent observations. Over the long integration period, minor errors in the ephemerides used to compensate Doppler changes become important, so to minimize image blurring, we apply phase-gradient autofocusing techniques [*Wahl et al*., 1984].

The high-resolution 70 cm images complement data collected at 3 μs delay resolution (500–600 m spatial resolution), which are calibrated to yield estimates of the dimensionless backscatter coefficient σ^0 with an uncertainty of ±3 dB (±50% in power) [*Campbell et al*., 2007]. We also have dual-polarization radar backscatter maps at 12.6 cm wavelength (2380 MHz frequency) with a single-look spatial resolution of about 40 m, which we average down to an 80 m resolution, four-look product. These observations are consistent in echo

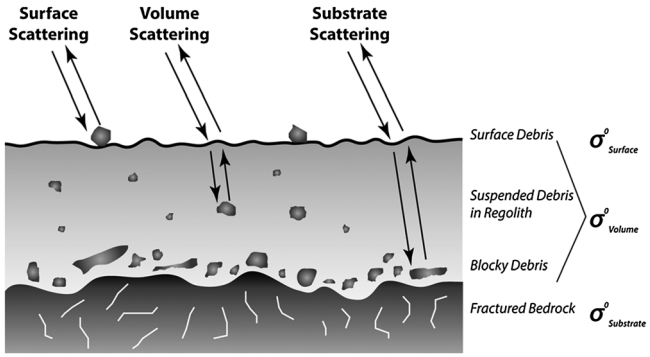

Figure 1. Cartoon of regolith physical structure and associated radar scattering mechanisms.

strength with respect to the transmitted power and background thermal noise but have not been fully calibrated to σ^0 [*Campbell et al.*, 2010].

3. Subsurface Radar Probing

3.1. Scattering Model

Radar backscatter from the lunar regolith arises from rocks on the surface, "volume" echoes from rocks suspended within the fine-grained debris, and reflections from the basal interface between the soil and the disrupted bedrock substrate (Figure 1). The latter two mechanisms are strongly affected by microwave losses associated with passage through the regolith material. At any radar wavelength, λ, we may express the observed backscatter coefficient as the sum of these three components:

$$\sigma^0 = \sigma^0_{\text{surface}} + \sigma^0_{\text{volume}} + \sigma^0_{\text{substrate}} \tag{1}$$

The notion of a single rough substrate interface is a proxy for the actual transition zone, which consists of mixed rubble and variable bedrock topography arising from the stochastic distribution of craters [e.g., *Shoemaker*, 1971]. It is likely that the radar-perceived roughness of the transition zone is not strongly dependent upon the original morphology of the mare-forming flows if the individual units are rarely more than 5 m thick [*Robinson et al.*, 2012], since several such layers might be disrupted and incorporated into the regolith after a few billion years.

The relative importance of each component to the overall echo varies considerably from $\lambda = 12.6$ cm to $\lambda = 70$ cm due to changes in the relevant rock populations and attenuation losses in the regolith. For example, surface rocks must have a diameter greater than about $\lambda/10$ to produce significant radar echoes. Most fragmental distributions of rocks can be described by a power law cumulative form, where $N(d)$, the number of rocks per unit area larger than diameter d, is proportional to d^{-s}, where s is a scaling coefficient related to the comminution of the debris. The wavelength dependence of radar echoes from these surface rocks is approximately λ^{2-s} [*Thompson et al.*, 1970]. Based on typical values of $s = 2.5$ to $s = 3.0$, the 70 cm radar echo from surface rocks will be 50% to 80% smaller than the 12.6 cm return, and we assume that most of the echoes at the longer wavelength arise from below the surface. The volume scattering also scales with the size-frequency distribution of suspended rocks, but we do not attempt here to characterize the dependence of this echo component on λ.

Both the volume and basal-interface components are modulated by the microwave loss tangent, the ratio of the imaginary component of the complex dielectric permittivity to the real component ($\tan\delta = \varepsilon''/\varepsilon'$), of the lunar soil. We can examine the impact of loss variations with a simple model of a soil layer of thickness h, with uniform volumetric rock population as a function of depth, overlying a rough interface that represents the transition to fractured, in-place bedrock (Figure 1). Echoes from the basal region are attenuated by passage through the soil [*Campbell*, 2002]:

$$\sigma^0_{\text{substrate}} = \sigma^0_{\text{vacuum}} T^2 R \exp[-4\alpha h/\cos\theta] \tag{2}$$

where σ^0_{vacuum} is the backscatter coefficient of an interface of equivalent roughness exposed at the surface, T is the Fresnel transmission coefficient of the regolith/vacuum interface, R is a loss term related

to the diminished Fresnel normal reflectivity contrast between soil and rock versus rock and vacuum, and θ is the angle between the transmitted ray and the surface normal. The loss factor, α, is:

$$\alpha = \frac{2\pi}{\lambda}\left[\frac{\varepsilon'}{2}\left(\sqrt{1+\tan\delta^2}-1\right)\right]^{1/2} \approx \frac{\pi\sqrt{\varepsilon'}}{\lambda}\tan\delta \quad (3)$$

where the right-hand expression is a low-loss approximation appropriate for most lunar materials [*Ulaby et al.*, 1981]. The real dielectric constant of the first few centimeters of the regolith is about 2.7, so T^2 is ~0.86. Taking approximate values of $\varepsilon' = 8$ for the rocky material and $\varepsilon' = 3$ for the average over the increasingly packed soil with depth, R is ~0.25. For volume scattering by rocks suspended in the soil, the effect of the losses is averaged over the probing depth of the radar [*Campbell*, 2002]:

$$\sigma^0_{\text{volume}} = \sigma^0_{\text{rocks}}\frac{T^2\cos\theta}{4\alpha}\left[1-\exp\left(\frac{-4\alpha h}{\cos\theta}\right)\right] \quad (4)$$

where σ^0_{rocks} is the total backscatter coefficient of rocks of all relevant sizes ($d \approx \lambda/10$ or greater) within a unit volume. The increase in "radar-visible" scattering rocks at lower loss is captured by the value of the loss factor, α, in the denominator of the coefficient in 4, while the exponential term leads to an asymptotic behavior for the echo as the product of thickness and loss parameter increases.

Impact crater ejecta blankets illustrate how radar wavelength and regolith properties affect the relative importance of surface and subsurface echoes. Figure 2 presents a UV-VIS mosaic and 12.6 cm and 70 cm SC-polarized radar images of the region surrounding the 55 km diameter crater Aristillus in eastern Mare Imbrium. This crater and the nearby Autolycus (39 km) and Theaetetus (24 km) are all characterized by optically bright (Figure 2a), morphologically fresh continuous ejecta suggesting an age of up to ~2 Ga within the Copernican or Eratosthenian periods [*Ryder et al.*, 1991]. All three have enhanced 70 cm backscatter within their floors and proximal ejecta blankets, suggesting abundant decimeter- to meter-scale debris within the few meter probing depth of the radar signal (Figure 2c). There is much greater diversity in the radar brightness of ejecta blankets at 12.6 cm wavelength (Figure 2b), with Aristillus having a clear concentric region of enhanced returns and Autolycus and Theaetetus exhibiting much less prominent differences from the surrounding terrain. Even over these relatively young crater ages, micrometeorite bombardment rapidly breaks down rocks on and near the surface [e.g., *Horz and Cintala*, 1997], diminishing the diffuse radar scattering from the upper meter or two; more deeply buried rocks survive longer [*Thompson et al.*, 1979]. The diffuse scattering enhancement of the ejecta blanket thus declines more quickly with age for 12.6 cm signals than for the 70 cm signal, since the shorter-wavelength echo arises primarily from the rapidly rock-depleted upper 1–2 m.

3.2. Mare Dielectric Properties and Effects on Scattering

A crucial aspect of understanding the relative roles of the volume and substrate radar echoes at different wavelengths is the dependence of microwave attenuation ($\tan\delta$) on regolith composition. Laboratory dielectric measurements of Apollo samples, summarized by *Carrier et al.* [1991], merge data for terra (low iron, low titanium) and mare samples (moderate to high iron, widely varying titanium) by expressing their composition as the sum of weight percent TiO_2 and FeO. This leads to fits to the overall sample collection, such as that cited by *Olhoeft and Strangway* [1975] for 450 MHz frequency:

$$\log_{10}(\tan\delta) = 0.033(\%\text{TiO}_2 + \%\text{FeO}) + 0.231\rho - 3.061 \quad (5)$$

where ρ is the bulk density of the material (g/cm^3). Difficulties arise, however, in applying these relationships to the broad range of mare units on the near side. Equation (5) implies that FeO content will strongly modulate the losses of low-TiO_2 mare units, an effect not observed in regional studies of 70 cm radar echoes [*Campbell et al.*, 1997; *Fa and Wieczorek*, 2012]. It appears that this expression bridges a gap between losses in mare soils modulated primarily by ilmenite ($FeTiO_3$) [*Schaber et al.*, 1975] and losses in terra materials modulated by various other iron-bearing minerals. We thus assume for our modeling a dependence of mare-regolith $\tan\delta$ only on TiO_2. Mixtures of a single high-loss component in a low-loss medium, such as water in dry snow, exhibit an approximately linear relationship between the fraction of the lossy material and the imaginary part of the dielectric permittivity [e.g., *Shivola et al.*, 1985]. For a constant overall mare regolith density, this translates into a linear relationship with $\tan\delta$, which we characterize as follows:

$$\tan\delta = \tan\delta_0 + \kappa(\%\text{TiO}_2) \quad (6)$$

where κ is a scaling coefficient and $\tan\delta_0$ is the loss tangent of the soil as the ilmenite content approaches zero.

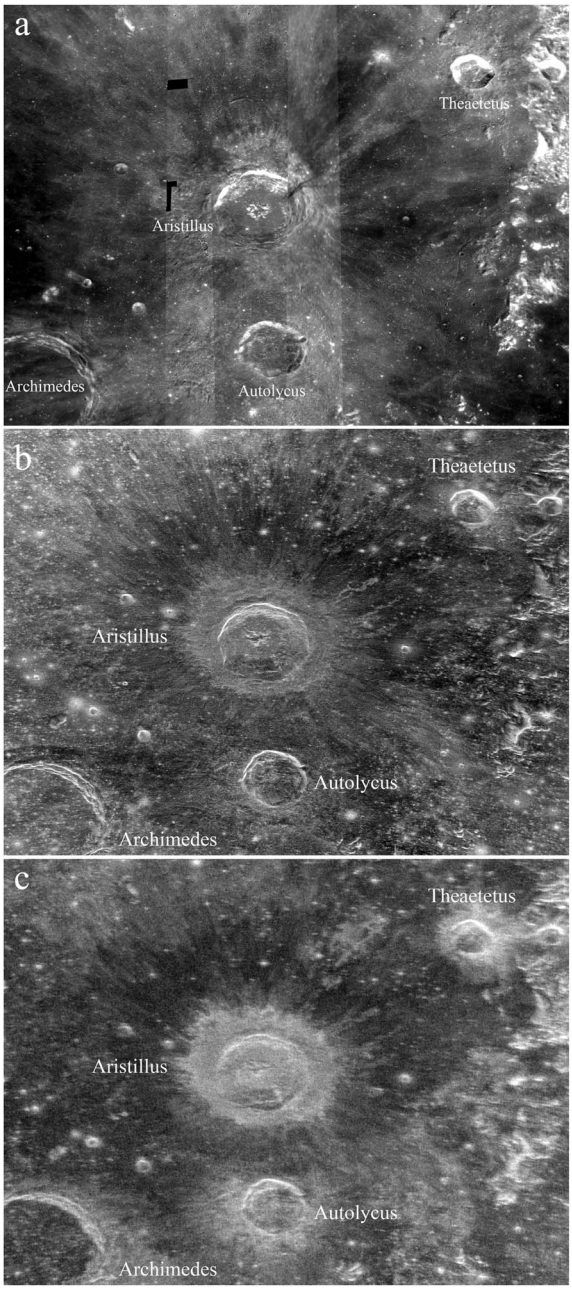

Figure 2. (a) Clementine 750 nm image mosaic for southeastern Mare Imbrium, highlighting the three young craters Aristillus, Autolycus, and Theaetetus. Image width about 400 km; cylindrical projection. (b) Same-sense circular polarization radar image at 12.6 cm wavelength for the same region. (c) Same-sense 70 cm wavelength radar image.

Lab-measured dielectric values for lunar samples provide constraints on these parameters. Plotting Apollo 11 through Apollo 17 mare soils and rock measurements of tan δ versus TiO_2 content [*Carrier et al.*, 1991], normalized to a density of 1.8 gm/cm^3, reveals a population for which the linear fit has significant uncertainty (Figure 3). A best fit function yields tan δ_0 of 0.0042 ± 0.0025. Most low-TiO_2 values ($<2\%$) fall below the linear fit, and there is likely a residual effect of trace contamination by terrestrial water, so tan δ_0 could be as low as 0.002. The slope of the best fit line, κ, is 0.0023 ± 0.0005.

The combination of κ and tan δ_0 determines (equations (2)–(4)) both the rate of change in the backscattered echo and the total attenuation loss associated with a particular regolith thickness and TiO_2 content. For the volume-scattered component, the maximum rate of change with TiO_2 abundance, about 1.5 dB per weight

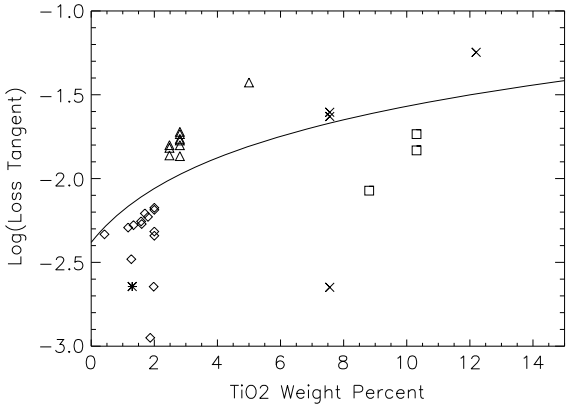

Figure 3. Loss tangent measurements for Apollo 11 through Apollo 17 mare soil and rock samples versus TiO_2 weight percentage. All values taken from *Carrier et al.* [1991, Table A9.16] and normalized to a density, ρ, of 1.8 g/cm^3, assuming that tanδ is proportional to $10^{0.3\rho}$. Sample 12065, a pigeonite basalt, is omitted here due to its anomalously high loss value. Solid line shows best fit linear function to the sample data (equation (5)). Plot symbols correspond to the following: Apollo 11 (crosses), Apollo 12 (triangles), Apollo 14 (asterisk), Apollo 15 (diamonds), Apollo 17 (squares).

percent, occurs for $\kappa = 0.003$ and $\tan\delta_0 = 0.002$ (Figure 4). Lower values of κ or higher values of $\tan\delta_0$ lead to smaller shifts in the backscatter with TiO_2 variations for a given population of suspended rocks. There is a significant effect of regolith thickness on the 70 cm returns, while the 12.6 cm echo is almost insensitive to thickness when $h > 5$ m.

Figure 5 shows the total 70 cm round-trip substrate loss with TiO_2 for regolith thickness from 5 m to 15 m, and two end-member combinations of $\tan\delta_0$ and κ. The sensitivity of the 12.6 cm echo to mare substrate reflections is negligible for regolith thickness exceeding a few meters due to the large total loss. The rate of change in the 70 cm substrate echo attenuation with TiO_2 (and its magnitude) rises dramatically with greater regolith thickness and increasing loss parameters, reaching 6 dB per weight percent at $h = 15$ m when $\kappa = 0.003$ and $\tan\delta_0 = 0.004$. Echoes from surface rocks will dampen the rate of change in overall echo strength (equation (1)) with loss-driven variations in the volume or substrate component (Figures 4 and 5), and this effect is more important at 12.6 cm than at 70 cm wavelength. Finally, we note that changes in regolith thickness for a given value of the loss tangent will also modulate the 70 cm substrate echo. Using our best fit parameters for $\tan\delta_0$ and κ yields a shift of about 2.0 dB in the round-trip attenuation, per meter of regolith thickness, when $TiO_2 < 4\%$.

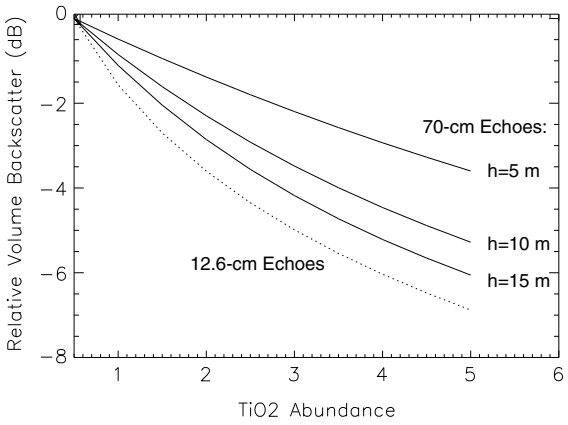

Figure 4. Plot of relative loss in radar backscatter power with increasing TiO_2 abundance for a volume distribution of rocks of thickness 5 m, 10 m, and 15 m. The 12.6 cm wavelength results, shown here for $h \sim 5$ m, are essentially independent of thickness over this range and are plotted as a single dashed curve. Slope $\kappa = 0.003$ and intercept $\tan\delta_0 = 0.002$ of the functional dependence of loss tangent on titanium weight percent. These parameters yield the maximum rate of change in loss, about 1.5 dB per weight percent TiO_2, for low titanium abundance.

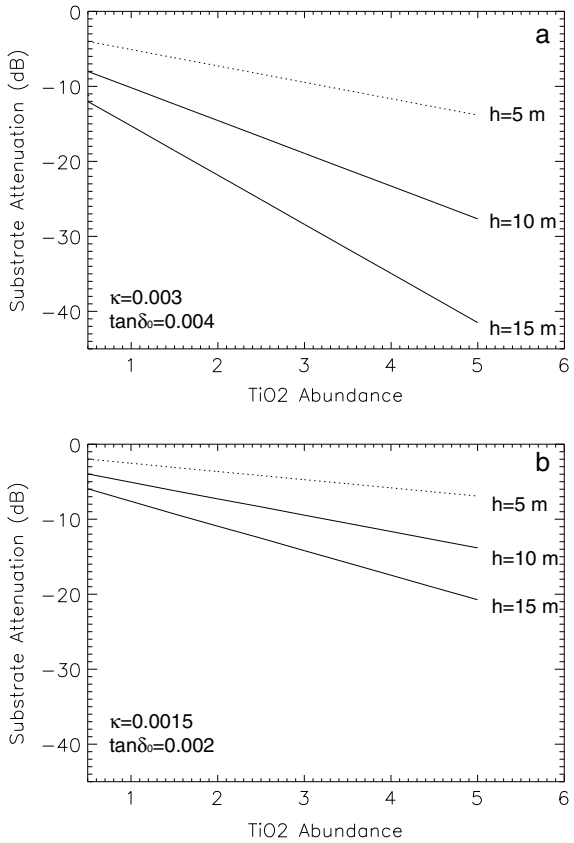

Figure 5. Total round-trip loss in 70 cm radar backscatter power with increasing TiO_2 abundance for a subsurface interface beneath regolith of thickness $h = 5$ m, 10 m, and 15 m. Example plots shown for two combination of the slope, κ, and intercept, $\tan\delta_0$, of the functional dependence of loss tangent on titanium weight percent (equation (5)): (a) $\kappa = 0.003$, $\tan\delta_0 = 0.004$; (b) $\kappa = 0.0015$, $\tan\delta_0 = 0.002$. The rate of change in echo strength with TiO_2 is much higher, up to 6 dB per weight percent, for a thicker regolith than for the volume component (Figure 4).

4. Remote Sensing Properties of Mare Serenitatis

An initial study found that parts of Mare Serenitatis exhibit stronger 70 cm SC backscatter and CPR than expected based on modeled values for their TiO_2 content and inferred that in these areas a significant echo component arises from well below the surface [*Campbell et al*., 2009]. Our new 70 cm data reveal much more detail of these anomalous radar-bright features, which comprise a broad region east of Bessel crater, a narrower region west of Bessel, a distinct north trending "fingered" deposit, and a separate area roughly parallel to the north margin of the basin (Figure 6). The hypothesis presented in the initial study was that the 70 cm radar returns are sensing local and regional variations in the roughness of the basal regolith interface, because maps of chemical composition using the model of *Lucey et al*. [2000] did not suggest an obvious correlation of lower radar echoes with enhanced TiO_2 abundance. In this section, we revisit the key issue of compositional variations, map the detailed patterns of scattering behavior at 12.6 cm and 70 cm wavelengths and assess unit ages and regolith depth based on small-crater abundance and ejecta properties. Section 5 integrates these results with the models presented in section 3 to offer a geologic scenario consistent with the observations.

Lava flow complexes in Mare Serenitatis span a wide range of age and record significant postemplacement deformation. In general, the flows comprising the surface units around the periphery of the basin are the oldest—up to 3.81 Ga, based on studies by *Hiesinger et al*. [2000]. The central and northern deposits have estimated ages of 3.4–3.5 Ga and are separated from the peripheral deposits by a concentric group of flow units of younger age. There are notable exceptions to this pattern, with isolated units along the basin edge as young as 2.44 Ga, and the anomalously younger (2.84 Ga) unit "S28" of *Hiesinger et al*. [2000] surrounded by much older material in east central Serenitatis. Studies of deformation patterns show that preserved graben are restricted to the mare and highland units along the outer margin of the Serenitatis basin [*Muehlberger*,

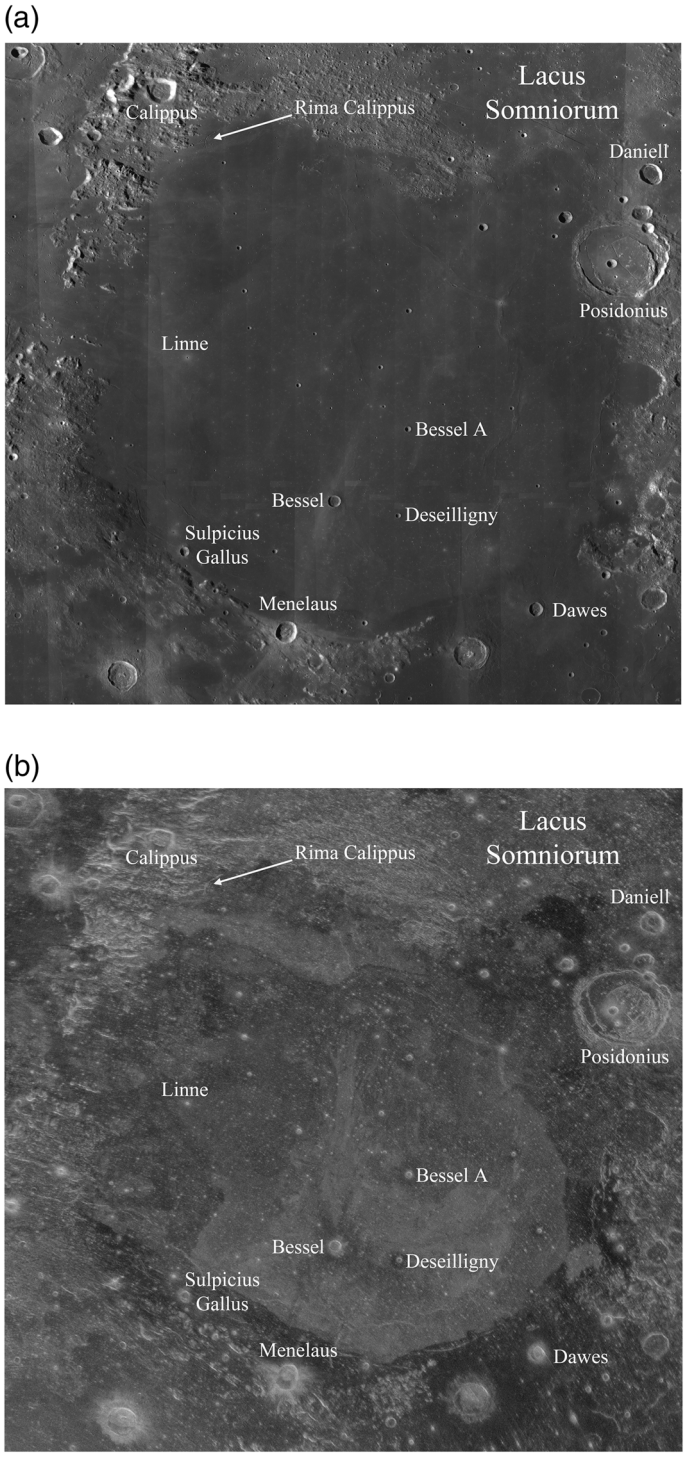

Figure 6. (a) Lunar Reconnaissance Orbiter Wide-Angle Camera visible image mosaic and (b) 70 cm wavelength, same-sense circular polarization radar image of Mare Serenitatis (14°N to 40°N, 4°E to 32°E). Image resolution 200 m per pixel; cylindrical projection with north toward top. LROC Wide-Angle Camera data from http://wms.lroc.asu.edu/lroc/view_rdr/WAC_GLOBAL.

1974; *Lucchitta and Watkins*, 1978], consistent with the end of extensional tectonism at 3.6 ± 0.2 Ga. Wrinkle ridges trend roughly north-south in the central basin, surrounded by a concentric pattern of ridges and gently tilted interridge areas. Ridge formation is generally agreed to postdate the eruption of mare

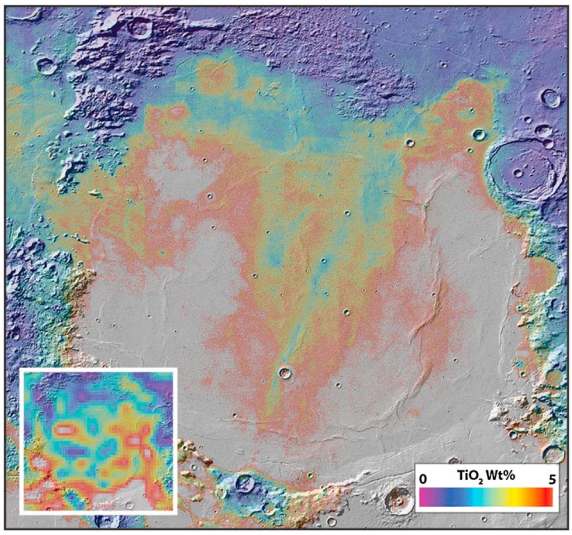

Figure 7. Estimated TiO_2 abundance based on method of *Lucey et al.* [2000], overlain on hillshade background of Mare Serenitatis, matching the region covered in Figure 6. Inset figure shows results to same color scale from the Lunar Prospector Gamma Ray Spectrometer analysis of *Prettyman et al.* [2006]. Topographic data from Lunar Reconnaissance Orbiter Wide-Angle Camera stereo processing [*Scholten et al.*, 2012].

basalts [*Fagin et al.*, 1978; *Watters and Konopliv*, 2001], suggesting that little information on regional slopes at the time of lava flow emplacement can be inferred from the current topography.

4.1. Compositional Properties

The radar-bright features in central Mare Serenitatis occur within a larger region of relatively low TiO_2 content, but the estimated absolute abundance of TiO_2 differs among various techniques. Using the *Lucey et al.* [2000] technique, based on Clementine UV-VIS measurements, yields a maximum of 4–6% TiO_2 across the central region (Figure 7), and the spatial pattern is not strongly correlated with the bright and dark regions of the 70 cm radar image (Figure 6b). The modified algorithm of *Gillis et al.* [2003] places all of central Mare Serenitatis at 2% or less TiO_2, with again little detailed correlation between the titanium abundance and changes in radar echo strength. A TiO_2 abundance of $<3\%$ across central Serenitatis was obtained with a hybrid model based on Lunar Prospector Gamma Ray Spectrometer (GRS) data and Neutron Spectrometer (NS) data [*Elphic et al.*, 2002]. In this map [*Elphic et al.*, 2002, Figure 9], however, there is a notable correlation between the shape of the high 70 cm backscatter regions in central Serenitatis (Figure 6b) and the area of lowest titanium abundance. A later analysis of the GRS data suggests values of $TiO_2 = 3$–4% across central Mare Serenitatis for the highest spatial resolution of 2°/pixel (Figure 7, inset) [*Prettyman et al.*, 2006]. All of the compositional models based on UV-VIS, gamma ray, or neutron measurements have significant uncertainties, reasonably estimated as $\pm 1\%$ in TiO_2. We thus take the 2–3% range of TiO_2 as a working description of central and northern Serenitatis flow units but allow for the possibility that variations of up to 1% in titanium abundance are not delineated by these techniques.

4.2. Backscatter Variations

We highlight in this section features from the regional 70 cm radar map (Figure 6b). Trending north from the region of Bessel crater is an almost straight-sided, radar-bright feature with finger-like termini (Figure 8a). In a 12.6 cm SC image (Figure 8b) these brightness changes are less evident, but portions of the north trending feature outlines (Figure 8c) can be discerned. Surrounding this feature in the 70 cm map are subparallel, elongate bright patches, as well as larger, more diffuse, radar-bright areas. Within the radar-bright regions are occasional radar-dark linear or arcuate features that are not correlated with the surface morphology (Figure 8c). The contacts between radar-bright patches and the extensive radar-dark material suggest embayment relationships, with the darker materials superposing parts of the bright terrain, and at least one brighter patch has a central radar-dark, sinuous feature. These patterns are similar to those of Venus flow fields, where lobate, radar-bright rough flows with central channels are partially superposed and flooded by

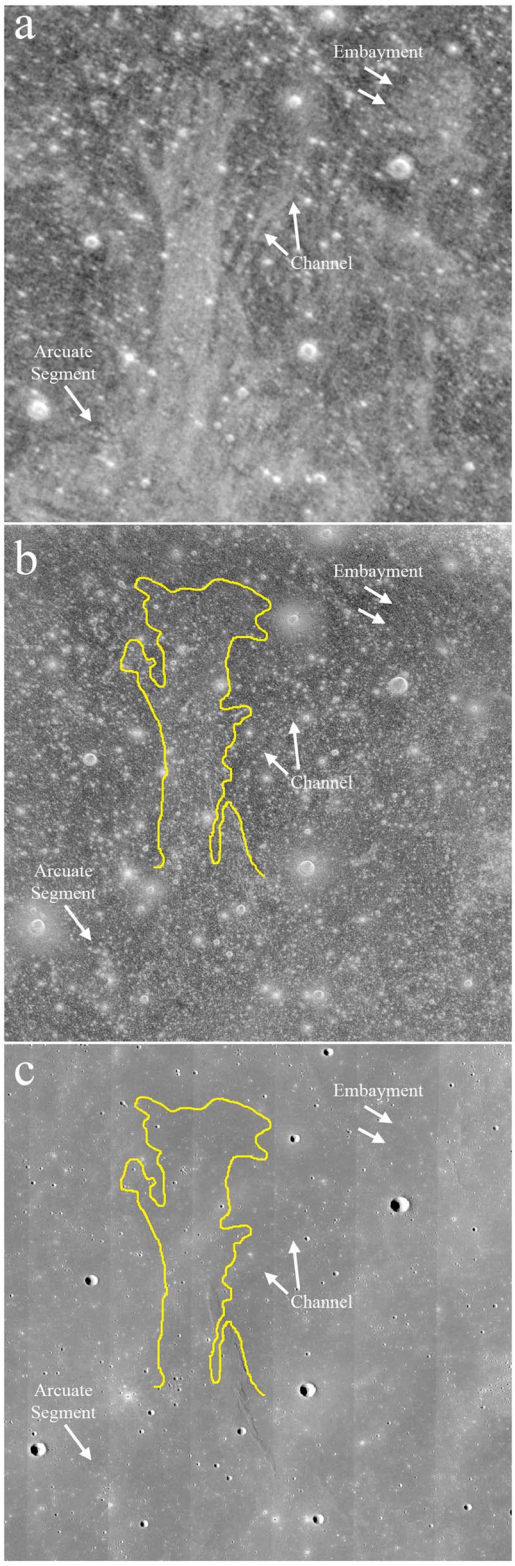

Figure 8. (a) Seventy centimeter wavelength, SC-polarized radar view of region north of Bessel crater. Image width is 225 km. Arrows and labels denote apparent embayment of radar-bright material by radar-dark material, a sinuous radar-dark channel, and one prominent arcuate radar-dark feature. Cylindrical projection with north toward top. (b) The 12.6 cm SC-polarized radar image of the same region. Note the subtle signature of higher radar brightness correlated with the north trending bright region in the 70 cm map. (c) LROC Wide-Angle Camera (WAC) visible image mosaic of the same region, with outline of area with high 70 cm radar echo noted. LROC Wide-Angle Camera data from http://wms.lroc.asu.edu/lroc/view_rdr/WAC_GLOBAL.

Figure 9. Magellan 12.6 cm radar image of lava flows north of Didilia Corona (approximate image center 19.6°N, 40.5°E). Image width 180 km and resolution 150 m per pixel. Note the rough-surfaced, radar-bright flows with central channels extending downhill from lower left of image. The bright flow at center has been bisected by later smooth (radar-dark) lava flows, which have also flooded the channels.

radar-dark, smooth flows (Figure 9) [*Campbell and Clark*, 2006]. The range in 70 cm SC brightness between the radar-bright and radar-dark regions has a maximum of 4–5 dB, or a factor of 2.5 to 3 in echo power.

To the west of Bessel, enhanced radar backscatter defines a 10–16 km wide, lobate feature that narrows and turns from a southwesterly direction to nearly due north (Figure 10). In the region east of Bessel, the margins of the radar-bright materials are rounded or broadly lobate. There are again modest variations in radar brightness over the region, typically with diffuse margins. An intriguing aspect of this region is a subparallel set of radar-dark linear or arcuate features with widths of 500–800 m (Figure 11). The dark features do not appear to be radar shadows cast by topography, despite their orientation roughly perpendicular to the look direction from the southwest and are not evident in the 12.6 cm SC image (Figure 12). A few may be distal parts of the radar-dark halo material of Bessel crater noted on Figure 11b [*Ghent et al.*, 2005], but most are not radial to Bessel or any other crater in the region, and thus have no immediate explanation as surficial deposits.

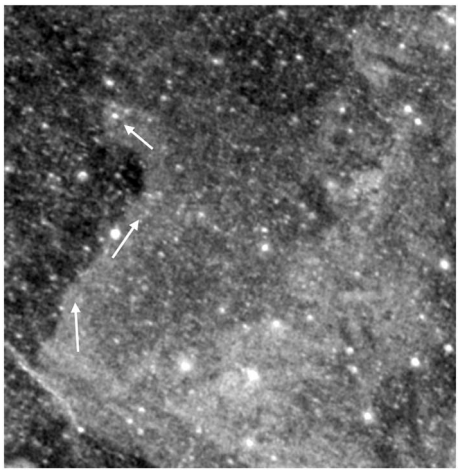

Figure 10. Seventy centimeter wavelength, SC-polarization image of a radar-bright feature west of Bessel crater. Note the lobate distal portion of this deposit. Image width 180 km. White arrows show inferred flow directions.

The radar-bright unit in northern Mare Serenitatis has a remarkable 250 km long, 1–3 km wide radar-dark feature along its southern margin (Figure 13). At the eastern end of the feature, the radar-dark signature appears to bisect the radar-bright materials. The radar-dark feature is correlated with a slight (~1%) increase in Clementine-derived TiO_2 abundance, but there is no significant shift in 12.6 cm radar echoes (Figure 13a, inset). Just to the northwest of this region is the local graben and fracture complex of Rima Calippus, which has associated patterns of lower 12.6 cm radar return (Figure 14). Such signatures are typical of localized pyroclastic deposits, and it appears that this mantling unit, extending up to about 2.5 km from the edge of the fractures, has not been previously mapped.

4.3. Relative Ages of Radar-Defined Units

The 70 cm SC radar image provides a complementary means of delineating surface units for

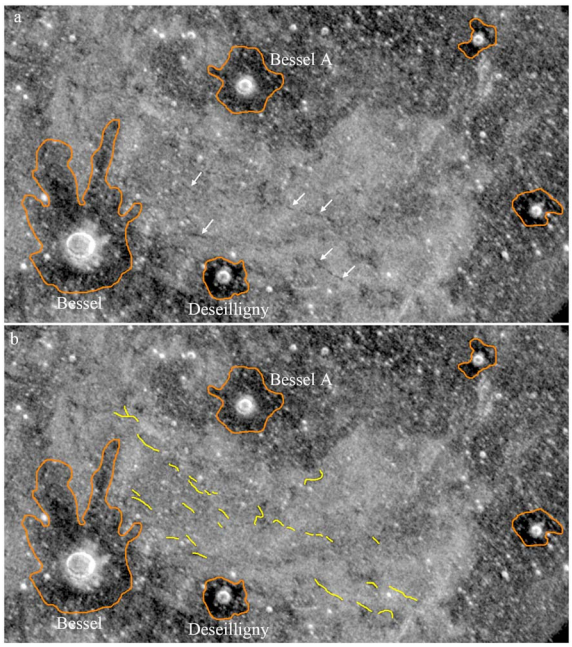

Figure 11. (a) A 70 cm wavelength, SC-polarization radar image of the region surrounding and east of Bessel crater. Image width 320 km. White arrows denote several prominent radar-dark arcuate or linear features. Orange outlines indicate approximate boundaries of radar-dark, fine-grained ejecta from nearby impact craters [*Ghent et al.*, 2005]. (b) Radar image labeled to show in yellow the location of all identified radar-dark linear and arcuate features within the broad, radar-bright deposits.

crater-population age dating, and thus a check on unit boundaries defined from UV-VIS properties [*Hiesinger et al.*, 2000]. In particular, the radar-bright region in eastern Mare Serenitatis is sufficiently extensive to permit an age estimate through crater size-frequency distributions. We divided this region into two areas (Figure 15) and counted all impact craters in the U.S. Geological Survey Lunar Orbiter mosaic greater than 500 m in diameter (58 total in 4966 km^2 of Area 1, 61 total in 4340 km^2 of Area 2). We did not attempt to identify secondary craters within these populations, so there is some additional uncertainty in our result. Matching the two cumulative crater populations (Figure 16) to the production functions of *Neukum et al.* [2001] yields surface ages of 3.40 Ga and 3.43 Ga.

Our overall region based on the radar-bright deposit margins (Figure 15) merges the "S15" and "S28" sample areas of *Hiesinger et al.* [2000], for which they obtained ages of 3.44 Ga and 2.84 Ga, respectively. We suggest

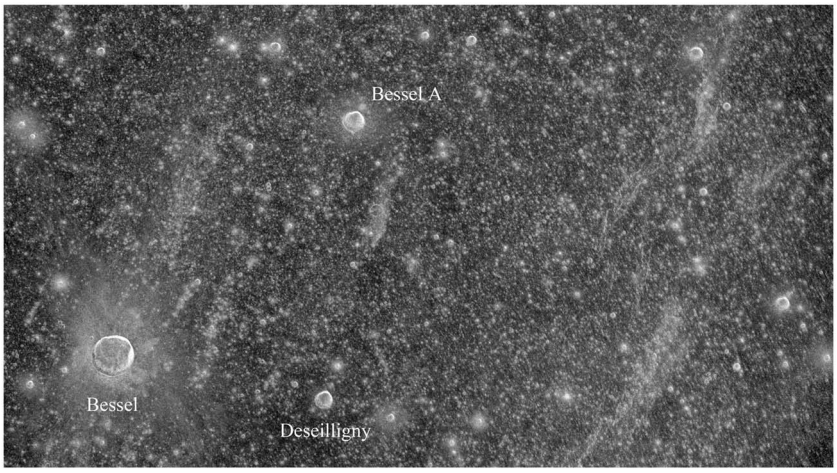

Figure 12. A 12.6 cm wavelength, SC-polarization radar image of the region surrounding and east of Bessel crater, approximately matching the coverage of Figure 11. There are no signatures similar to those of the radar-dark arcuate segments seen in the 70 cm, SC-polarization image. Spatial resolution is about 80 m per pixel.

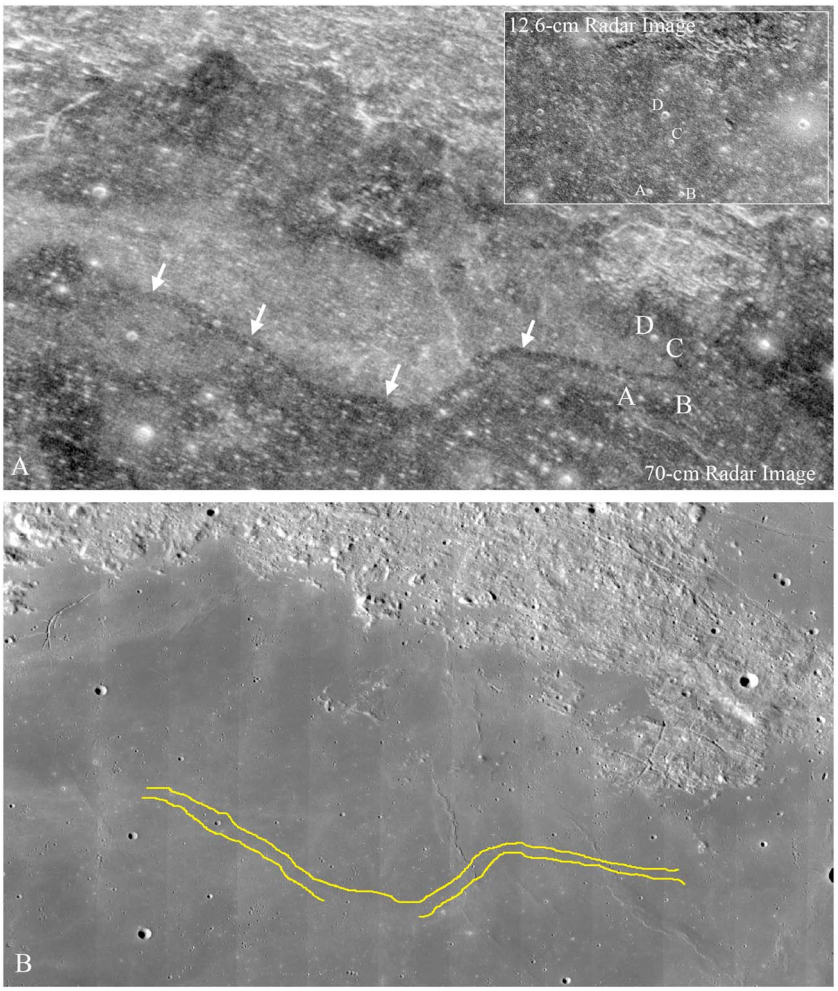

Figure 13. (a) A 70 cm wavelength, SC-polarization radar image of a radar-dark sinuous feature in northern Mare Serenitatis (white arrows). Image width 370 km. Inset shows 12.6 cm wavelength, SC-polarization radar image for a portion of this region. Note the lack of evidence for the radar-dark sinuous feature with the shallower penetration capability of the 12.6 cm signals. Four small craters are labeled A–D in both images for location reference. (b) LROC WAC visible image mosaic for the matching region, with the margins of the low 70 cm radar echoes shown. The location and shape of this feature suggest that the radar-dark materials filled and overflowed a preexisting graben. LROC Wide-Angle Camera data from http://wms.lroc.asu.edu/lroc/view_rdr/WAC_GLOBAL.

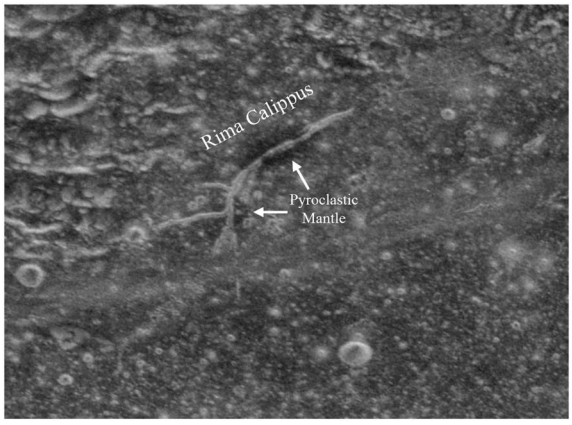

Figure 14. A 12.6 cm wavelength, same-sense circular (SC) polarization, radar image of the area surrounding Rima Calippus in northwestern Mare Serenitatis (Figure 6). Image width 90 km. The radar-dark features along the rille are inferred to be pyroclastic mantling deposits.

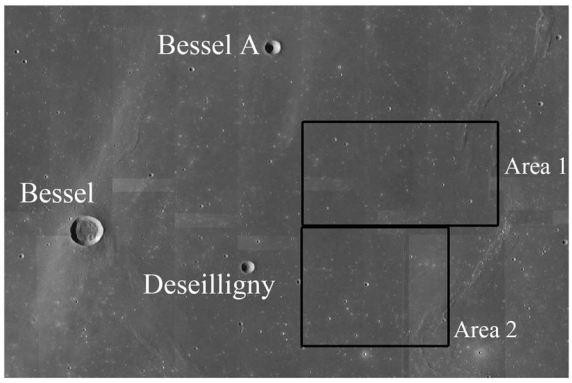

Figure 15. LROC WAC visible image mosaic of the region east of Bessel crater, showing the outlines of areas used to determine crater age dates. LROC Wide-Angle Camera data from http://wms.lroc.asu.edu/lroc/view_rdr/WAC_GLOBAL.

that the radar-based definition of sampling regions shows no need for splitting of the "S28" unit, which resulted in an apparent age much younger than all surrounding material and created difficulties in interpreting regional basalt stratigraphy [*Weider et al.*, 2010]. The ages of the two radar-defined regions east of Bessel are very similar to that of unit "S17" (3.43 Ga), which closely follows the radar-bright elongate deposit in northern Mare Serenitatis (Figure 13). An upper end age estimate of 3.49 Ga comes from the "S13" region that covers much of the radar-bright unit north and west of Bessel crater. Surrounding units have estimated ages of 2.9–3.3 Ga [*Hiesinger et al.*, 2000]. For the purpose of constraining regolith thickness variations, our radar-bright and radar-dark unit boundaries might thus be associated with age differences between flow complexes of ~5% of their estimated ages (e.g., ~0.2 Ga).

4.4. Regolith Thickness

The thickness of the regolith on mare surfaces has been studied since the first Surveyor landings, and simple models for excavation and comminution of initial bedrock suggest considerable variability in thickness above a rugged interface or blocky zone [*Shoemaker*, 1971; *Horz and Cintala*, 1997]. Estimates of the average depth of the soil still differ widely, with lower end values of about 5 m supported by studies of benches and outcrops in small craters. Greater values were inferred from studies of the Apollo landing sites, including a 14 m estimate on mare units at Apollo 17 [*Wolfe et al.*, 1981]. A 15–30 m thickness range comes from analysis of ejecta blocks surrounding small fresh craters, assuming an excavation depth about 14% the final diameter of the cavity [*Wilcox et al.*, 2005]. Remote-sensing models have been developed to address thickness variations, but the

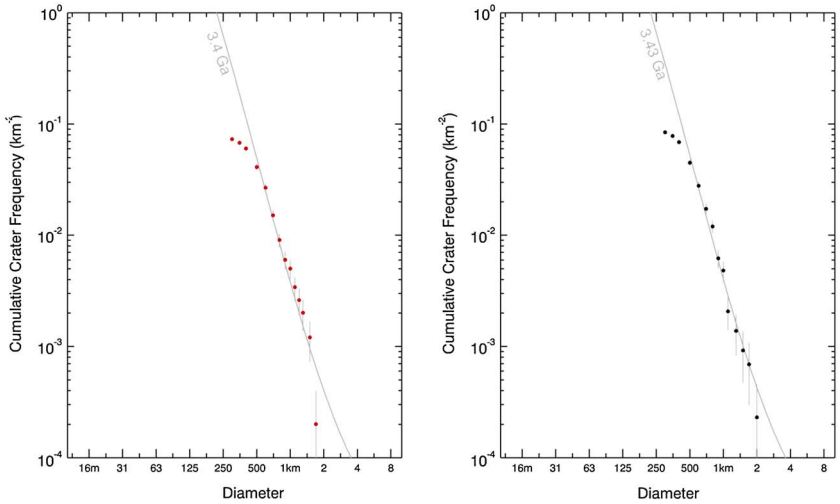

Figure 16. Cumulative population plots for impact craters in two subregions of Mare Serenitatis; (left) Area 1 and (right) Area 2 noted in Figure 15. Crater production functions for age estimation from *Neukum et al.* [2001], with craters in diameter bins from 0.5 to 1.7 km included in the fits.

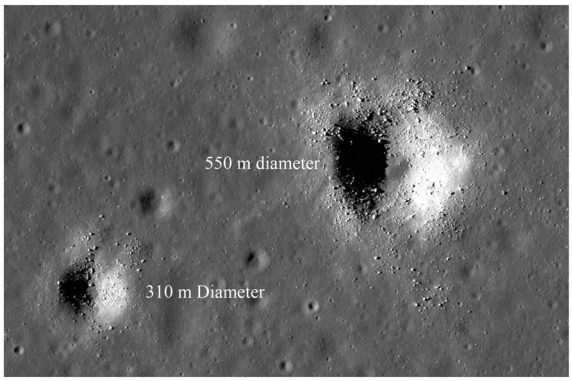

Figure 17. Portion of LROC NAC visible image frame M181037901LC, showing two craters with abundant meter scale and larger boulders in their ejecta. Sun angle is 69°. Image width is about 2.5 km.

absolute depth calibration is often linked to values derived from photogeologic methods. For example, a model based on 70 cm backscatter data, Clementine UV-VIS estimates of FeO and TiO_2, and a 5 m typical mare regolith thickness, led to an estimate of ~4 m for Mare Serenitatis [*Shkuratov and Bondarenko*, 2001].

In order to provide an independent estimate of regolith thickness in our study area, we applied the method of *Wilcox et al.* [2005] to a region northeast of Bessel crater, using Lunar Reconnaissance Orbiter Camera (LROC) Narrow Angle Camera (NAC) frames M181037901L and R [*Robinson et al.*, 2010]. We counted the craters within this ~940 km^2 region that have significant numbers of meter-scale blocks within their ejecta or on their interior walls (Figure 17). Of the 126 total, the smallest bouldery craters had D ~ 100 to 150 m, but only a fraction of craters in this diameter range appear to have excavated such debris. A much larger percentage of craters $>$200 m in diameter have blocky ejecta. Plotting the craters in a size-frequency format and fitting a power law to the values for D $>$ 200 m, we estimate that only about 20% of the expected population of young 100–200 m craters have blocky ejecta. Using the 14% relationship between diameter and excavation depth proposed by *Wilcox et al.* [2005] suggests that a large fraction of the regolith in this part of Mare Serenitatis is 10–15 m thick, with rapidly diminishing areal coverage by thicker deposits. This result is supported by the presence of several 100–150 m diameter, bright-ejecta craters across the study area with no apparent associated blocky material.

5. Modeling and Conclusions

The 70 cm radar map reveals a high degree of spatial variability in backscatter properties within an area of generally low TiO_2 content (Figures 6 and 7). Planform outlines of these radar backscatter differences are strongly suggestive of lava flow unit boundaries, embayment relationships, and channel-like features. Remote-sensing data, the Apollo sample dielectric measurements, and our models for regolith radar scattering in section 3 constrain possible explanations for these observations. First, we can assert that the changes in 70 cm echo power between the "bright" and "dark" units in central and northern Mare Serenitatis do not primarily reflect changes in the surface or volume distribution of rocks within the upper meter or two of the soil. Any such changes would lead to a similar scaling of 12.6 cm and 70 cm SC radar echoes, whereas we observe only modest variations in 12.6 cm returns. Likewise, changes in soil TiO_2 content lead to similar rates of change at both radar wavelengths for their volume-scattering echo components (Figure 4). The reasonable conclusion is that small variations in soil TiO_2 content and/or thickness create strong variability in 70 cm echoes from the rugged transition zone at the base of the regolith. A similar situation occurs in radar studies of the Aristarchus Plateau where 70 cm signals penetrate pyroclastic deposits to reveal areas of lava flooding [*Campbell et al.*, 2008], and the 12.6 cm echoes are enhanced only where the mantling is thin.

Based on NS, GRS, and UV-VIS data, we adopt a typical value of 2–3% for TiO_2 abundance, and allow for a range of 1% in possible "undetected" variation between lava flow complexes. Based on the modeling in section 3, we note that a 1% change in TiO_2 weight percent abundance corresponds to about 2 dB of substrate echo change for 5 m regolith thickness, increasing to 4 dB for 10 m thickness and 6 dB for 15 m thickness. In each case, the overall 70 cm echo variation is diminished by the less dramatic response of the volume-scattered component to changes in TiO_2 (Figure 4), so the estimated regolith thickness is a lower limit. The observed SC-polarized, 70 cm backscatter

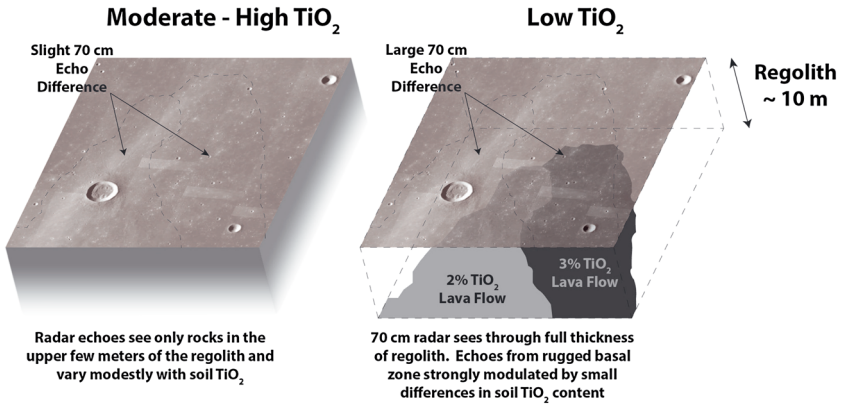

Figure 18. Cartoon of proposed mechanism for differences in radar backscatter among mare units in this study. (left) At moderate to high (~4% or more) titanium abundance, both 12.6 cm and 70 cm wavelength echoes see only the surface and suspended rocks within the regolith. (right) At low (less than about 4%) TiO_2 abundance, the 70 cm echo can have a strong component from the rugged transition zone between the soil and the intact bedrock.

coefficients differ by 4–5 dB between the "radar-dark" and "radar-bright" parts of north central Mare Serenitatis. If we are constrained to a 1% variation in TiO_2, with no variability in regolith age/thickness, then the regolith thickness must be 10 m or greater to provide adequate radar-echo sensitivity to the small change in composition.

Figure 18 presents a cartoon representation of our proposed scenario. For moderate to high TiO_2 content, neither wavelength "sees" the rugged transition zone at the base of the regolith, and echo changes in response to small differences in ilmenite content are modest. Once the regolith losses are low enough to allow a strong substrate echo to occur, any small shift in TiO_2 content has a much more significant effect on the 70 cm echo due to the long round-trip propagation path. Under these conditions, the radar map becomes a very sensitive tool for delineating subtle differences in ilmenite content between flow units.

Could a plausible rough transition zone, buried by the regolith, produce the observed backscatter power, given round-trip losses? This is difficult to answer due to uncertainties in the absolute values of the 70 cm backscatter coefficient (±3 dB) [*Campbell et al*., 2007], mare TiO_2 content (assumed to be 2% to 3%, but perhaps even lower) [*Gillis et al*., 2003], and parameters of the regolith loss function (e.g., $\tan\delta_0$ as low as 0.002). With a thick regolith, even minor reductions in $\tan\delta$ translate into large shifts in total round-trip substrate loss. Using our best fit values from the Apollo samples ($\tan\delta_0 = 0.0042$, $\kappa = 0.0023$) and adding the reflectivity (6 dB) and transmission (1 dB) losses (section 3), a 10 m thick regolith with $TiO_2 = 2\%$ will impose a total round-trip loss of -22 dB. Changes in regolith thickness with age, at the 5% level, contribute no more than about 1 dB variation in the 70 cm echo for the 10 m case.

From the earlier 70 cm data, we measure SC backscatter coefficients of -28 ± 3 dB, at 40° to 44° incidence, for the radar-bright northern "finger" unit (Figure 8a) [*Campbell et al*., 2007]. The substrate interface echo, if exposed at the surface, would thus have to be -6 ± 3 dB. Values of about -8 dB define the upper end of measured SC backscatter coefficients for very rugged terrain on Mars [e.g., *Harmon et al*., 1999], so the premise of a substrate-echo scenario for the Mare Serenitatis radar-bright areas is at least within the realm of possibility for a 10 m regolith. Slightly lower values for $\tan\delta_0$ and/or the TiO_2 content of the radar-bright regions would reduce the required value of σ^0_{vac} and permit potentially greater regolith thickness.

The variations in 70 cm backscatter, which we suggest are due to a high sensitivity of the radar echo to small changes in TiO_2 abundance in low-titanium regions where the substrate echo can play a major role (Figure 18), offer a rare opportunity to see details of flow complexes within the maria. These flows exhibit a range of morphologic styles, from broad, sheet-like deposits west of Bessel (Figure 11) to locally lobate and channelized features in north central Mare Serenitatis (Figure 8). We noted in section 4 the apparent similarity between radar brightness patterns seen in north central Serenitatis and those of flow complexes on Venus, but the long linear western margin of the radar-bright finger north of Bessel (Figure 8) is not typical of such flow field contacts. One possibility is that this margin is due to early folding or fracturing of the mare materials as wrinkle ridge formation began, creating a topographic barrier against which one or both of the flow units

ponded. The trend of this linear contact is in keeping with the general north-south alignment of deformation in the central basin [*Fagin et al*., 1978; *Watters and Konopliv*, 2001].

The radar-dark feature that rings the southern edge of the high-return region in northern Mare Serenitatis has a shape and location with respect to the basin topography consistent with a graben that has been infilled by mare flow materials of the slightly higher-TiO_2 variety. There are low radar-return mare units at the east and west ends of this feature, so the infilling could have come from either direction. *Lucchitta and Watkins* [1978] note the likelihood that circumferential graben formed during the period between basin formation and about 3.6 ± 0.2 Ga, with those interior to the basin margins filled by later mare lavas. The 2–3 km maximum width of the feature is larger than those mapped in nearby Lacus Somniorum (Figure 6a), so this may imply a degree of overtopping of the graben channel by the lavas.

The radar-dark lineaments east of Bessel (Figure 11) seem too narrow and localized to be higher-TiO_2 flows that flood earlier lava channels. They may represent locally deeper regolith cover due to slumping into gaps or voids, and by analogy with recent observations of mare pits and subsurface voids [*Robinson et al*., 2012] might be collapsed portions of once-subsurface lava tubes. Future work will test these inferences through detailed correlation of topography and any subtle changes in surface morphology evident in low Sun-angle photos with radar-mapped flow and channel features. We also have 70 cm radar coverage for Mare Imbrium, Mare Crisium, and Mare Humorum that will yield additional insight into variations in lunar basalt flow field morphology and eruption conditions.

Acknowledgments

The authors thank J. Cahill and an anonymous reviewer for their thoughtful comments on the manuscript. This work was supported in part by grants from NASA's Planetary Astronomy and Planetary Geology and Geophysics Programs. The authors thank the staff at Arecibo Observatory and the Green Bank Telescope for invaluable assistance in collecting the lunar radar data. John Chandler of the Smithsonian Astrophysical Observatory provided the lunar ephemerides for our mapping. Mark Cintala offered helpful comments during our consideration of models for regolith structure. The Arecibo Observatory is operated by SRI International under a cooperative agreement with the National Science Foundation (AST-1100968), and in alliance with Ana G. Méndez-Universidad Metropolitana, and the Universities Space Research Association. The Arecibo Planetary Radar Program is supported by the National Aeronautics and Space Administration under grant NNX12AF24G issued through the Near Earth Object Observations program. The Green Bank Telescope is part of the National Radio Astronomy Observatory, a facility of the NSF operated under cooperative agreement by Associated Universities, Inc.

References

Campbell, B. A. (2002), *Radar Remote Sensing of Planetary Surfaces*, pp. 331 , Cambridge Univ. Press, New York.

Campbell, B. A. (2012), High circular polarization ratios in radar scattering from geologic targets, *J. Geophys. Res.*, *117*, E06008, doi:10.1029/2012JE004061.

Campbell, B. A., and D. A. Clark (2006), Geologic map of the Mead Quadrangle (V-21), Venus, U.S. Geological Survey Atlas of Venus, *Sci. Inv. Map 2897*.

Campbell, B. A., B. R. Hawke, and T. W. Thompson (1997), Long-wavelength radar studies of the lunar maria, *J. Geophys. Res.*, *102*, 19,307–19,320.

Campbell, B. A., D. B. Campbell, J. L. Margot, R. R. Ghent, M. Nolan, J. Chandler, L. M. Carter, and N. J. S. Stacy (2007), Focused 70-cm radar mapping of the Moon, *IEEE Trans. Geosci. Remote Sens.*, *45*(12), 4032–4042, doi:10.1109/TGRS.2007.906582.

Campbell, B. A., L. M. Carter, B. R. Hawke, D. B. Campbell, and R. R. Ghent (2008), Volcanic and impact deposits of the Moon's Aristarchus Plateau: A new view from Earth-based radar images, *Geology*, *36*, 135–138, doi:10.1130/G24310A.1.

Campbell, B. A., B. R. Hawke, L. M. Carter, R. R. Ghent, and D. B. Campbell (2009), Rugged lava flows on the Moon revealed by Earth-based radar, *Geophys. Res. Lett.*, *36*, L22201, doi:10.1029/2009GL041087.

Campbell, B. A., L. M. Carter, D. B. Campbell, M. Nolan, J. Chandler, R. R. Ghent, B. R. Hawke, R. F. Anderson, and K. Wells (2010), Earth-based S-band radar mapping of the Moon: New views of impact melt distribution and mare physical properties, *Icarus*, doi:10.1016/j.icarus.2010.03.011.

Carrier, W. D., Olhoeft, G. R., and W. Mendell (1991), Physical properties of the lunar surface, in *Lunar Sourcebook*, edited by G. Heiken, D. T. Vaniman, and B. M. French pp. 475-594, Cambridge Univ. Press, New York.

Elphic, R. C., D. J. Lawrence, W. C. Feldma, B. L. Barraclough, O. M. Gasnault, S. Maurice, P. G. Lucey, D. T. Blewett, and A. B. Binder (2002), Lunar Prospector neutron spectrometer constraints on TiO_2, *J. Geophys. Res.*, *107*(E4), 5024, doi:10.1029/2000JE001460.

Evans, J. V. (1968), Modulation, demodulation, and data processing applied to radar astronomy, in *Radar Astronomy*, chap. 9, edited by T. Hagfors and J. V. Evans pp. 499-545, McGraw-Hill, New York, 620 pp.

Fa, W., and Y. Jin (2010), A primary analysis of microwave brightness temperature of lunar surface from Chang-E 1 multi-channel radiometer observation and inversion of regolith layer thickness, *Icarus*, doi:10.1016/j.icarus.2009.11.034.

Fa, W., and M. A. Wieczorek (2012), Regolith thickness over the lunar nearside: Results from Earth-based 70-cm Arecibo observations, *Icarus*, *218*, 771–787, doi:10.1016/j.icarus.2012.07.008.

Fagin, S. W., D. M. Worral, and W. R. Muehlberger (1978), Lunar mare ridge orientations: Implications for lunar tectonic models, *Proc. Lunar. Planet. Sci. Conf.*, *9*, 3473–3479.

Ghent, R. R., D. W. Leverington, B. A. Campbell, B. R. Hawke, and D. B. Campbell (2005), Earth-based observations of radar-dark crater haloes on the Moon: Implications for regolith properties, *J. Geophys. Res.*, *110*, E02005, doi:10.1029/2004JE002366.

Gifford, A. W., and F. El-Baz (1981), Thickness of lunar mare flow fronts, *Earth Moon Planets*, *24*, 391–398.

Gillis, J. J., B. L. Joliff, and R. C. Elphic (2003), A revised algorithm for calculating TiO_2 from Clementine UVVIS data: A synthesis of rock, soil, and remotely sensed TiO_2 concentrations, *J. Geophys. Res.*, *108*(E2), 5009, doi:10.1029/2001JE001515.

Harmon, J. K., R. E. Arvidson, E. A. Guiness, B. A. Campbell, and M. A. Slade (1999), Mars mapping with delay-Doppler radar, *J. Geophys. Res.*, *104*, 14,065–14,089.

Head, J. W. (1975) Lunar mare deposits: Areas, volumes, sequence, and application for melting in source areas, Conference on Origins of Mare Basalts and Their Implications for Lunar Evolution, Lunar Science Institute, Houston, 66–71.

Hiesinger, H., R. Jaumann, G. Neukum, and J. W. Head (2000), Ages of basalts on the lunar nearside, *J. Geophys. Res.*, *105*, 29,239–29,275.

Hiesinger, H., J. W. Head, U. Wolf, R. Jaumann, and G. Neukum (2003), Ages and stratigraphy of mare basalts in Oceanus Procellarum, Mare Nubium, Mare Cognitum, and Mare Insularum, *J. Geophys. Res.*, *108*(E7), 5065, doi:10.1029/2002JE001985.

Horz, F., and M. Cintala (1997), Impact experiments related to the evolution of planetary regoliths, *Meteorit. Planet. Sci.*, *32*, 179–209.

Le Mouelic, S., Y. Langevin, S. Erard, P. Pinet, S. Chevrel, and Y. Daydou (2000), Discrimination between maturity and composition of lunar soils from integrated Clementine UV-visible/near-infrared data: Application to the Aristarchus Plateau, *J. Geophys. Res.*, *105*, 9445–9455, doi:10.1029/1999JE001196.

Lucchitta, B. K., and J. A. Watkins (1978), Age of graben systems on the Moon, *Proc. Lunar Planet. Sci. Conf.*, *9*, 3459–3472.

Lucey, P. G., D. T. Blewett, and B. D. Joliff (2000), Lunar iron and titanium abundance algorithms based on final processing of Clementine UV-Visible images, *J. Geophys. Res.*, *105*, 20,297–20,306.

Muehlberger, W. R. (1974), Structural history of southeastern Mare Serenitatis and adjacent highlands, *Proc. Lunar. Planet. Sci. Conf.*, *5*, 101–110.

Murase, T., and A. R. McBirney (1973), Properties of some common igneous rocks and their melts at high temperatures, *Geol. Soc. Am. Bull.*, *84*, 3563–3592.

Neukum, G., B. Ivanov, and W. Hartmann (2001), Cratering records in the inner solar system in relation to the lunar reference system, *Space Sci. Rev.*, *96*, 55–87.

Oberbeck, V., and W. Quaide (1968), Genetic implications of lunar regolith thickness variations, *Icarus*, *9*, 446–465.

Olhoeft, G. R., and D. W. Strangway (1975), Dielectric properties of the upper 100 m of the Moon, *Earth Planet Sci. Lett.*, *24*, 394–404.

Prettyman, T. H., J. J. Hagerty, R. C. Elphic, W. C. Feldman, D. J. Lawrence, G. W. McKinney, and D. T. Vaniman (2006), Elemental composition of the lunar surface: Analysis of gamma ray spectroscopy data from Lunar Prospector, *J. Geophys. Res.*, *111*, E12007, doi:10.1029/2005JE002656.

Quaide, W. L., and V. R. Oberbeck (1968), Thickness determinations of the lunar surface layer from lunar impact craters, *J. Geophys. Res.*, *73*, 5247–5270.

Quaide, W., and V. Oberbeck (1975), Development of the mare regolith: Some model considerations, *The Moon*, *13*, 27–55.

Robinson, M. S., et al. (2010), Lunar Reconnaissance Orbiter Camera (LROC) instrument overview, *Space Sci. Rev.*, *150*, 81–124, doi:10.1007/s11214-010-9634-2.

Robinson, M. S., J. W. Ashley, A. K. Boyd, R. V. Wagner, E. J. Speyerer, B. R. Hawke, H. Hiesinger, and C. H. van der Bogert (2012), Confirmation of sublunarean voids and thin layering in mare deposits, *Planet. Space Sci.*, *69*, 18–27, doi:10.1016/j.pss.2012.05.008.

Ryder, G., D. Bogard, and D. Garrison (1991), Probable age of Autolycus and calibration of lunar stratigraphy, *Geology*, *19*, 143–146.

Schaber, G. G. (1973), Lava flows in Mare Imbrium: Geologic evaluation from Apollo orbital photography, *Proc. Lunar. Planet. Sci. Conf. 4*, *1*, 73–92.

Schaber, G. G., T. W. Thompson, and S. H. Zisk (1975), Lava flows in Mare Imbrium: An evaluation of anomalously low Earth-based radar reflectivity, *The Moon*, *13*, 395–423.

Scholten, F., J. Oberst, K.-D. Matz, T. Roatsch, M. Wahlisch, E. J. Speyerer, and M. S. Robinson (2012), GLD100: The near-global lunar 100 m raster DTM from LROC WAC stereo image data, *J. Geophys. Res.*, *117*, E00H17, doi:10.1029/2011JE003926.

Shivola, A., E. Nyfors, and M. Tiuri (1985), Mixing formulae and experimental results for the dielectric constant of snow, *J. Glaciol.*, *31*, 163–170.

Shkuratov, Y. G., and N. V. Bondarenko (2001), Regolith layer thickness mapping of the Moon by radar and optical data, *Icarus*, *149*, 329–338, doi:10.1006/icar.2000.6545.

Shoemaker, E. M. (1971), Origin of fragmental debris on the lunar surface and history of bombardment of the Moon, *Univ. de Barcelona*, *XXV*, 26–56.

Takeda, H., M. Miyamoto, T. Ishii, and G. E. Lofgren (1975), Relative cooling rates of mare basalts at Apollo 12 and 15 sites as estimated from pyroxene exsolution data, Proc. Lunar Sci. Conf. 6th, 987–996.

Thompson, T. W., J. B. Pollack, M. J. Campbell, and B. T. O'Leary (1970), Radar maps of the Moon at 70-cm wavelength and their intepretation, *Radio Sci.*, *5*, 253–262.

Thompson, T. W., W. J. Roberts, W. K. Hartmann, R. W. Shorthill, and S. H. Zisk (1979), Blocky craters: Implications about the lunar megaregolith, *Moon Planets*, *21*, 319–342.

Ulaby, F. T., R. K. Moore, and A. K. Fung (1981), *Microwave Remote Sensing*, vol. 1, p. 456, Addison-Wesley, Reading, MA.

Wahl, D. E., P. H. Eichel, D. C. Ghiglia, and C. V. Jakowatz (1984), Phase gradient autofocus—A robust tool for high resolution SAR phase correction, *IEEE Trans. Aerosp. Electron. Syst.*, *30*, 827–835.

Watters, T. R., and A. S. Konopliv (2001), The topography and gravity of Mare Serenitatis: Implications for subsidence of the mare surface, *Planet. Space Sci.*, *49*, 743–748.

Weider, S. Z., I. A. Crawford, and K. H. Joy (2010), Individual lava flow thicknesses in Oceanus Procellarum and Mare Serenitatis from Clementine multispectral data, *Icarus*, *209*, 323–336, doi:10.1016/j.icarus.2010.05.010.

Weill, D. F., R. A. Grieve, I. S. McCallum, and Y. Bottinga (1971), Mineralogy-petrology of lunar samples. Microprobe studies of samples 12021 and 12022; viscosity of melts of selected lunar compositions, Proc. Lunar Sci. Conf. 2nd, 413-430.

Wilcox, B. B., M. S. Robinson, P. C. Thomas, and B. R. Hawke (2005), Constraints on the depth and variability of the lunar regolith, *Meteorit. Planet. Sci.*, *40*, 695–710.

Wolfe, E. W., N. G. Bailey, B. K. Lucchitta, W. R. Muehlberger, D. H. Scott, R. L. Sutton, and H. G. Wilshire (1981), The geologic investigation of the Taurus-Littrow Valley: Apollo 17 landing site, *USGS Prof. Pap.*, *1080*, 280.

Wu, Y., B. Xue, B. Zhao, P. Lucey, J. Chen, Z. Xu, C. Li, and Z. Ouyang (2012), Global estimates of lunar iron and titanium contents from the Chang' E-1 IIM data, *J. Geophys. Res.*, *117*, E02001, doi:10.1029/2011JE003879.